

Conditional Adversarial Camera Model Anonymization

Jerone T. A. Andrews, Yidan Zhang, and Lewis D. Griffin

Department of Computer Science, University College London
jerone.andrews@cs.ucl.ac.uk

Abstract. The model of camera that was used to capture a particular photographic image (model attribution) is typically inferred from high-frequency model-specific artifacts present within the image. Model anonymization is the process of transforming these artifacts such that the apparent capture model is changed. We propose a conditional adversarial approach for learning such transformations. In contrast to previous works, we cast model anonymization as the process of transforming both high and low spatial frequency information. We augment the objective with the loss from a pre-trained dual-stream model attribution classifier, which constrains the generative network to transform the full range of artifacts. Quantitative comparisons demonstrate the efficacy of our framework in a restrictive non-interactive black-box setting.

Keywords: Camera model anonymization, conditional generative adversarial nets, adversarial training, non-interactive black-box attacks, image editing/manipulation, camera model attribution/identification

1 Introduction

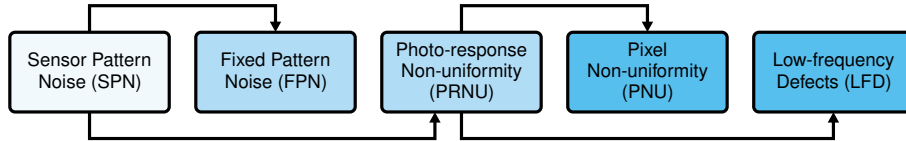
Photographic images can be attributed to the specific camera model used for capture [29]. Attribution is facilitated by inferring model-specific digital acquisition and processing artifacts present within high-frequency pixel patterns [64,54,25,30,65,4]. While such artifacts have been used to verify the origin and integrity of images, attribution evidently raises concerns about unjustifiable misuse. This is particularly pertinent to individuals such as human rights' activists, photojournalists and whistle-blowers, that reserve the right to privacy and anonymity [23].

In this work, we are not concerned with attribution per se, but the challenging problem of camera model anonymization [14,51,42]. Model anonymization is the process of transforming model-specific artifacts s.t. the apparent capture model is changed. Namely, the goal is to learn a function that transforms the innate model-specific artifacts of an image to those of a disparate target model. Such a system could then be used to preserve privacy, or conversely for validating the robustness and reliability of attribution methods, particularly when attribution results are admitted as forensic evidence in civil or criminal cases.



Light enters the imaging device via a system of lenses and optical filters. The CFA mosaic projects each pixel to a color: R, G or B. The sensor output is a single-channel mosaic representation. In order to obtain an RGB color image, color interpolation (a.k.a. demosaicing) estimates the missing color information in each channel based on neighboring pixels. Preceding digital storage, the image undergoes various post-processing (e.g. white balancing, color correction, gamma correction, compression).

Fig. 1. Simplified digital image acquisition pipeline



Imaging SPN is defined as any noise component that survives frame averaging [38]—i.e. systematic distortions—and primarily comprises of FPN and PRNU. FPN is defined as the pixel-to-pixel differences when the sensor is not exposed to light [49], whereas PRNU is the dominant component of SPN. PRNU is largely caused by PNU, which is defined as stochastic variations in the sensitivity of individual pixel sensors to light. Finally, LFD are artifacts that change slowly in intensity over long spatial distances (e.g. optical vignetting). LFD are a result of the lens and camera optics, as opposed to the imaging sensor.

Fig. 2. Imaging sensor pattern noise sources

Broadly, previous work on model anonymization tend to view anonymization as *solely* necessitating the attenuation [51,10] or transformation [14,15,21] of the device-specific pixel non-uniformity imaging sensor noise [26], which is defined as slight variations in the sensitivity of individual pixel sensors. Although initially device-specific (prior to color interpolation), these variations propagate nonlinearly through the processing steps (Fig. 1) that result in the final image and thus end up also depending on model-specific aspects, such as color interpolation, on-sensor signal transfer, sensor design and compression [27].

Pixel non-uniformity is the dominant noise component of what is termed photo-response non-uniformity (Fig. 2). Photo-response non-uniformity noise, however, also contains contributions from low spatial frequency artifacts (independent of the imaging sensor) caused by light refraction on dust particles, optical surfaces and properties of the camera model optics [48]. Such artifacts include optical vignetting [46], which corresponds to the fall-off in light intensity towards the corners of an image.

Model anonymization approaches based on pixel non-uniformity invariably suppress the noise-free imaging sensor response (image content), via a denoising filter, and instead work with the *noise residual* (the observed image minus its estimated noise-free image content). This is premised on improving the signal-to-noise ratio between the photo-response non-uniformity noise (signal of interest) and the observable image. However, this precludes the anonymization process from attending to discriminative low spatial frequency model-specific artifacts, since they no longer exist within the high-frequency noise residual.

Despite model anonymization loosely falling under the remit of image editing [58,66,69], the targeted anonymizing transformations that we seek should not alter the image content of an input. Minimal distortion is easily achieved by formulating the problem as a lossy reconstruction task, however low distortion is often at odds with high perceptual quality [7]. We therefore absorb the lossy reconstruction task into a simple adversarial training procedure, taking inspiration from conditional generative adversarial networks [57]. The gist of the procedure is that the generator transforms (with low distortion) an input image conditioned on a target camera model label, and tries to fool the discriminator into thinking the transformed image’s prediction error features (low-level high-frequency pixel value dependency features) are real and coherent with the condition.

In contrast to previous work, we cast model anonymization as the process of transforming both high and low spatial frequency model-specific artifacts. With this in mind, our conditional adversarial camera model anonymizing (Cama) framework also includes a fixed (w.r.t. its parameters) dual-stream discriminative decision-making component (evaluator) that decides whether a transformed image belongs to its target class. Each stream captures a different aspect of the input data. Specifically, we decompose an input into its high and low spatial frequency components and assign each to its own stream. The intuition is that this allows the evaluator to *independently* reason over specific information present in each. Augmenting the adversarial objective with the evaluator’s *discriminative* objective reinforces the transformation process and ensures that both high and low spatial frequency model-specific artifacts are attended to by the generator.

Quantitative results underscore the efficacy of our framework when attacking a variety of non-interactive black-box target classifiers, irrespective of whether an input image was captured by a camera model *known* to our framework.

1.1 Related Work

Camera Model Attribution. Classical approaches to camera model attribution typically construct parametric models of particular physical or algorithmic in-camera processes [20,25,19,13,6,64]. Others operate *blindly*, viewing attribution as a texture classification problem, and derive a set of heuristically designed features irrespective of their physical meaning [55,44,30,67]. Recent methods based on deep learning take a data-driven approach, obviating the need for explicit prior domain knowledge [5,47,9,65,4]. A common thread unifying most classical and contemporary approaches is image content suppression (employed as a preprocessing step) [64,54,25,30,65,4]. That is, it is *a priori* assumed that model-specific image acquisition and processing artifacts are wholly contained in the high-frequency pixel non-uniformity noise (corrupted by in-camera processes) as opposed to the low-frequency image content. Notwithstanding, it has been empirically shown [62] that this preprocessing step is not strictly necessary when the model attribution classifier is a sufficiently deep convolutional neural network (convnet), i.e. training may be performed directly in the spatial domain. Here we focus on deceiving convnet classifiers—with and without image content suppression—which can be considered state-of-the-art.

Camera Model Anonymization. As a direct consequence of the fixation of model attribution methods on model-specific artifacts contained within the pixel non-uniformity noise, model anonymization methods have mostly focused on attenuating or misaligning these high-frequency micro-patterns. Notable approaches include flat-fielding [32,8], pixel non-uniformity estimation and subtraction [42,22,10], irreversible forced seam-carving [23], image patch replacement [24] and image inpainting [51]. However, a principal issue with the aforementioned approaches is the detectable absence of model-specific artifacts within the anonymized images [11]. In contrast, we *transform* the underlying model-specific artifacts of images rather than distorting them.

Adversarial Examples. In image classification, adversarial examples refer to misclassified inputs obtained by applying imperceptible non-random perturbations [63]. Such attacks are well studied and are typically categorized based on the knowledge available to the adversary (as well as whether the attack causes an untargeted or targeted misclassification). Broadly, white-box attacks require complete knowledge (architecture and parameters) of the classifier to be attacked, whereas black-box attacks require only partial knowledge (obtained by querying the targeted classifier). Similar to other image classification tasks, recent research has shown that model attribution convnets are also extremely vulnerable to adversarial examples, particularly in white-box scenarios [36,53,15,21]. Nevertheless, in the challenging black-box setting, there are clear issues w.r.t. the transferability of adversarial examples [53,21]. In fact, the apparent lack of transferability has been echoed in other image forensic classification tasks [2,35], such as median filtering and resizing detection, which is in stark contrast to what has been observed in classical object-centric classification tasks.

Generative Adversarial Networks. Generative adversarial networks (GANs) [33] offer a viable framework for training generative models and are increasingly being used for tasks such as image generation [43], image editing [69] and representation learning [56]. Extending this framework to conditional image generation applications, conditional GANs (cGANs) [57] have been successfully applied to image-to-image translation [70,40,71] and modifying image attributes [58,68]. Most relevant to our work are the approaches of MISL [14,15] and SpoC [21], which both propose *multiple* camera model anonymizing (unconditional) GANs with access to a single fixed evaluator. That is, for each target camera model, a separate (generator, discriminator) tuple is trained, thus markedly increasing the computational cost. Moreover, MISL only considers the transformation of high-frequency artifacts contained within noise residuals. Differently, SpoC *implicitly* aims to transform image- and noise residual-based artifacts. Using a fixed preprocessor, the discriminative networks (including the evaluator) receive as input the original image concatenated channel-wise with its noise residual. The main problem with concatenating these modalities is that it does not necessarily constrain the discriminative networks to reason over the specific information present in each. Notably, neural networks are known to take *shortcuts* [28], and

we posit that the discriminative networks learn to rely almost entirely on the noise residual components, as this high-frequency information is not obfuscated by the non-discriminative image content (leading to faster convergence).

2 Method

In this section, we outline the attack setting and desiderata, and explain the motivation and core components of our conditional adversarial camera model anonymizer (Cama). Refer to Appendix A for an extended motivation.

2.1 Attack Setting and Desiderata

We denote by $x \in \mathbb{R}^d$ and $y \in \mathbb{N}_c = \{1, \dots, c\}$ an image and its ground truth (source) camera model label, respectively, sampled from a dataset p_{data} . Consider a *target* (i.e. to be attacked) convnet classifier F with c classes trained over input-output tuples $(x, y) \sim p_{\text{data}}(x, y)$. Given x , F outputs a prediction vector of class probabilities $F : x \mapsto F(x) \in [0, 1]^c$.

In this work, we operate in a *non-interactive black-box setting*: we do not assume to have knowledge of the parameters, architecture or training randomness of F , nor can we interact with it. We do, however, assume that we can sample from a dataset similar to p_{data} , which we denote by q_{data} . Precisely, we can sample tuples of the following form: $(x, y) \sim q_{\text{data}}(x, y)$ s.t. $y \in \mathbb{N}_{c'}$, where $c' \leq c$. That is, the set of possible image class labels in p_{data} is a superset of the set of possible image class labels in q_{data} , i.e. $\mathbb{N}_c \supseteq \mathbb{N}_{c'}$.

Suppose $(x, y) \sim q_{\text{data}}(x, y)$ and $y' \in \mathbb{N}_{c'}$, where $y' \neq y$ is a target label. Our aim is to learn a function $G : (x, y') \mapsto x' \approx x$ s.t. the maximum probability satisfies $\arg \max_i F(x')_i = y'$. This is known as a *targeted* attack, whereas the maximum probability of an *untargeted* attack must satisfy $\arg \max_i F(x')_i \neq y'$. This work focuses on targeted attacks.

2.2 Cama: Conditional Adversarial Camera Model Anonymizer

In this framework, our model has two class conditional components: a generator G that transforms an image x conditioned on a target class label y' , and a discriminator D that predicts whether the low-level high-frequency pixel value dependency features of any given image conditioned on a label are real or fake. In addition, our model has a fixed (w.r.t. its parameters) dual-stream discriminative decision-making component E (evaluator) that decides whether a transformed image x' belongs to its target class y' . In essence, E serves as a *surrogate* for the non-interactive black-box F . W.r.t. E , a transformed image x' is decomposed into its high and low spatial frequency components (x'_H and x'_L , respectively), via E_0 , with each assigned to a separate stream (E_H and E_L , respectively). The evaluator then reasons over the information present in x'_H and x'_L separately (via E_H and E_L , respectively). This reinforces the transformation process, as G is constrained

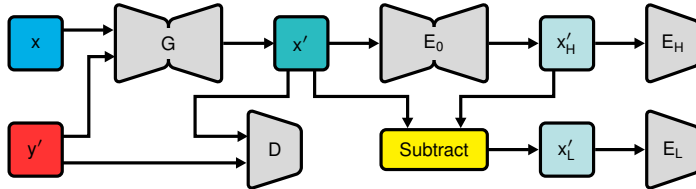


Fig. 3. Flow diagram of our method Cama given an input tuple (x, y')

to transform both high and low spatial frequency camera model-specific artifacts used by the evaluator for discrimination. Cama is illustrated in Fig. 3.

Our objective contains three types of terms: an *adversarial loss* for matching the distribution of transformed images to the data distribution q_{data} ; a *pixel-wise loss* to incentivize the preservation of image content; and a *classification loss* to encourage G to apply transformations that result in transformed images lying in their respective target classes.

Adversarial Loss. To learn plausible conditional transformations, we apply an adversarial loss to G . For G and D , the training process alternates between G minimizing

$$L_{\text{adv}} = \mathbb{E}_{\substack{x \sim q_{\text{data}}(x) \\ y' \sim q_{\text{data}}(y)}} \left[(D(x', y') - 1)^2 \right], \quad (1)$$

and D minimizing

$$L_{\text{dis}} = \mathbb{E}_{(x, y) \sim q_{\text{data}}(x, y)} \left[(D(x, y) - 1)^2 \right] + \frac{1}{2} \left[\mathbb{E}_{\substack{x \sim q_{\text{data}}(x) \\ y' \sim q_{\text{data}}(y)}} \left[D(x', y')^2 \right] + \mathbb{E}_{\substack{x \sim q_{\text{data}}(x) \\ y' \sim q_{\text{data}}(y)}} \left[D(x, y')^2 \right] \right]. \quad (2)$$

Note that this is the matching-aware [59] least squares formulation [52] of the generative adversarial objective [33], which offers increased learning stability, generates higher quality results and encourages G to output images *aligned* with their target labels.

In this work, the first layer of the discriminator is a *constrained* convolutional layer [3] (originally proposed for image manipulation detection), which learns a set of prediction error filters. Each filter’s central value is constrained to equal -1 , whereas its remaining elements are constrained to sum to unity. In other words, the constrained layer extracts prediction error features (low-level high-frequency pixel value dependency features) by learning a normalized linear combination of the central pixel value based on its local neighborhood [4]. This concurrently serves to suppress image content.

Pixel-Wise Loss. Although D constrains G to learn credible transformations, it does not ensure that an input image’s content is preserved. To incentivize this,

we incorporate a simple pixel-wise L^1 norm loss between x' and x :

$$L_{\text{pix}} = \mathbb{E}_{\substack{x \sim q_{\text{data}}(x) \\ y' \sim q_{\text{data}}(y)}} [\|x - x'\|_1]. \quad (3)$$

The addition of this loss tasks G with producing images that are close to the ground truth input image, i.e. $x' \approx x$. We prefer an L^1 norm loss over an L^2 norm loss since it has been observed to encourage less blurring [70].

Classification Loss. Ideally, x' should possess all relevant target model-specific artifacts that are the result of in-camera processes, i.e. artifacts associated with y' . However, the previously introduced adversarial and pixel-wise losses give no guarantees as to whether x' lies in class y' according to an attribution classifier such as F . In particular, as G is guided by D , the adversarial game may fixate on discovering and fixing peculiarities in x' such as abnormal interpolation patterns [1,17]. This could result in a failure to transform the *range* of salient model-specific (high and low spatial frequency) artifacts learned by a discriminative classifier, i.e. $\arg \max_i F(x')_i \neq y'$. To evaluate and reinforce the transformation process, we adopt a pre-trained fixed dual-stream camera model attribution convnet classifier E , where E is employed as a *proxy* for F . To decompose an input image x' into its high and low spatial frequency components, the evaluator is prefixed with a preprocessor (convnet) $E_0 : x \mapsto E_0(x') = x'_H$, where x'_H is the high-frequency noise residual of x' . The low spatial frequency components are computed as $x'_L = x' - x'_H$. Formally, given x' we propose to reduce the expected negative log-likelihood w.r.t. y' by minimizing

$$L_{\text{clf}} = -\frac{1}{2} \mathbb{E}_{\substack{x \sim q_{\text{data}}(x) \\ y' \sim q_{\text{data}}(y)}} [\log (E_H(x'_H)_{y'} E_L(x'_L)_{y'})], \quad (4)$$

where E_H and E_L denote the high and low spatial frequency streams of E , respectively. Incorporating this loss into the generative objective encourages G to update its parameters s.t. the predicted class of x' is y' according to both streams of E .

Full Objective. The full generative objective is as follows:

$$L_{\text{gen}} = L_{\text{adv}} + \lambda_{\text{pix}} L_{\text{pix}} + \lambda_{\text{clf}} L_{\text{clf}}, \quad (5)$$

where λ_{pix} and λ_{clf} are weights that control the contribution of the three objectives. The discriminative objective is as outlined in Eq. (2).

3 Implementation

To facilitate reproducibility, we make our code publicly available.¹

¹ <https://github.com/jeroneandrews/cama>

Table 1. Dataset itemization. Shown are the number of images per class within each set

y	Camera Model	Set		
		q_{data}	p_{data}	p_{test}
1	Kodak M1063	760	765	100
2	Casio EX-Z150	324	335	100
3	Nikon CoolPixS710	352	330	100
4	Praktica DCZ5.9	345	358	100
5	Olympus mju-1050SW	374	379	100
6	Ricoh GX100	353	296	100
7	Rollei RCP-7325XS	–	339	100
8	Panasonic DMC-FZ50	–	677	100
9	Samsung NV15	–	396	100
10	Samsung L74wide	–	432	100
11	Fujifilm FinePixJ50	–	397	100
12	Canon Ixus70	–	333	100
Total		2508	5037	1200

Dataset. To provide a comparison on a prevalent digital image forensics benchmark, we use the Dresden image database [31] of RGB .jpeg images. Specifically, we use a subset of images from 12 camera models centrally cropped to a common resolution of 512×512 . We partition the images into three disjoint sets (Table 1), which are disjoint w.r.t. the specific devices used to capture the images. Throughout, sets q_{data} , p_{data} , and p_{test} are used for constructing non-interactive black-box attacks, target classifier training, and evaluating attack methods, respectively.

Network Architecture. The generative network is adapted from [41] and contains two residual blocks. Following [14], prior to being fed to the network, an input image $x \in \mathbb{R}^d$ is preprocessed (using the Bayer ‘RGGB’ pattern) s.t. it is projected to a color filter array mosaic pattern and then back to a demosaiced RGB image. This serves to remove an input image’s original demosaicing traces and forces the generator to *re-demosaic* its input w.r.t. the target camera model condition. The preprocessed image and target label condition $y' \mapsto \{0, 1\}^d$ are then concatenated in the channel dimension, where the y' -th channel of a target condition is filled with ones with the remaining channels filled with zeros. The discriminative network is adapted from [40] and operates at patch-level by classifying 34×34 overlapping input patches as real or fake. The constrained convolutional layer has three 5×5 filters with stride and zero-padding equal to 1 and 2, respectively, s.t. the output of this layer retains the spatial size of its input. Similar in principle to [58], label conditions are reshaped and concatenated in the filter dimension of the output of the first *standard* convolutional layer. The evaluator’s preprocessor E_0 employs the same underlying architecture as G , whereas each stream (i.e. E_H and E_L) uses a ResNet-18 architecture [37].

Training Details. For training, we perform data augmentation by extracting non-overlapping 64×64 patches from 512×512 images $\sim q_{\text{data}}$ and using dihedral group Dih_4 transformations. We first train E_0 to approximate ground truth noise residuals obtained through wavelet-based Wiener filtering.² We minimize an L^2 norm loss for 90 epochs using Adam [45] with default parameters, learning rate $1e-4$, weight decay $5e-4$ and batch size 128. Fixing E_0 , we separately train E_H and E_L to minimize a negative log-likelihood loss. We train both for 90 epochs using SGD with momentum 0.9, initial learning rate 0.1, weight decay $5e-4$ and batch size 128. Fixing the modules of E , we empirically set $\lambda_{\text{pix}} = 10$

² We refer the reader to [26] for details on this denoising filter.

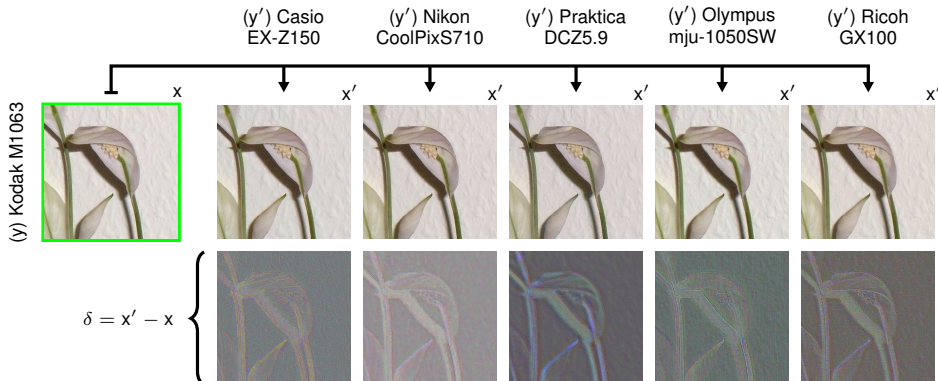


Fig. 4. Example of Cama transformed images x' with different target label conditions y' given an in-distribution input image x . The applied transformations (amplified for visualization purposes) are shown as δ

and $\lambda_{\text{clf}} = 0.01$ in Eq. (5). We optimize Cama for 200 epochs using the Adam solver with learning rate $2e-4$, momentum parameter $\beta_1 = 0.5$ and batch size 32.

4 Experiments

In this section, we provide evidence supporting our main claims: (i) model anonymization requires the transformation of both high and low spatial frequency artifacts, and (ii) better anonymization performance can be obtained by employing an adversarial evaluator that reasons over specific information present in a transformed image’s high and low spatial frequency components *separately*.

4.1 Experimental Setup

All networks used in this work are fully-convolutional, therefore we can both classify and anonymize images of arbitrary size. Evaluation is always performed on 512×512 images $\sim p_{\text{test}}$. Fig. 4 illustrates Cama’s ability to transform an input image using different target label conditions. The applied transformations do not alter the image content and are (largely) imperceptible. See Appendix B for additional qualitative results on both in-distribution and out-of-distribution images.

Baselines. To contextualize our approach, we compare against several baselines quantitatively. From the GAN literature (Section 1.1), we recast the unconditional approaches MISL [14,15] and SpoC [21] as cGANs. The evaluator of MISL has a single-stream and is prefixed with a constrained convolutional layer. The discriminator and single-stream evaluator of SpoC use a fixed preprocessor, which concatenates an RGB image and its third-order finite differences channel-wise. To

ensure a fair comparison, we implement the baselines using the same architecture and details as Cama (where appropriate), and set the parameters of all methods s.t. the mean peak signal-to-noise ratio is approximately 35dB. See Appendix C for additional comparisons to targeted attack methods from the adversarial examples literature (and mean peak signal-to-noise ratios when anonymizing images $\sim p_{\text{test}}$). We omit these from the main body due to space limitations and their poor performance in contrast to the selected baselines.

Target Classifiers. To validate the efficacy of Cama, we vary the architecture of a target camera model attribution classifier F , its prefixed preprocessor and its training data ($\sim p_{\text{data}}$). Namely, we consider ResNet-18 [37], ResNet-50 [37], DenseNet-100 [39] and VGG-16 [61] architectures. Regarding the preprocessors, image content suppression is performed by fixed hand-crafted high-pass filtering (HP) [65], third-order finite differencing (FD) [21], constrained convolution filtering (CC) [3] or wavelet-based Wiener filtering (WW) [26]. We also consider the channel-wise concatenation of an RGB image with its third-order finite differences (RGB+FD) [21]. No preprocessing is simply denoted by RGB. For training, F is trained over tuples $\sim p_{\text{data}}(x, \mathbb{N}_6)$ or $p_{\text{data}}(x, \mathbb{N}_{12})$. We refer to the former as a *complete overlap* and the latter as a *partial overlap* of known camera model classes.³ The training details (e.g. training epochs, optimizer, data augmentation, etc.) are the same as used for our evaluator streams (described in Section 3). To confirm that the classifiers F can perform accurate camera model attribution, we compute their classification accuracy on relevant non-anonymized images $\sim p_{\text{test}}$. We obtain a mean accuracy of 99.5%, which varies by 1.5% from one target classifier to the next.

Evaluation Measures. We consider the targeted success rate (TSR) for evaluating the anonymization ability of a non-interactive black-box attack, which is defined as the fraction of all possible x' that satisfy $\arg \max_i F(x')_i = y'$. For completeness, we also report the untargeted success rate (USR), i.e. the fraction of x' that satisfy $\arg \max_i F(x')_i \neq y$. We report these rates separately for in-distribution images (i.e. captured by camera models *known* to an attack framework) and out-of-distribution images (i.e. captured by camera models *unknown* to an attack framework). The best scores are always shown in boldface.

4.2 Results

Same Architecture Complete Overlap. We first analyze the success rates against ResNet-18 target classifiers F trained over $(x, y) \sim p_{\text{data}}(x, \mathbb{N}_6)$. Recall that the evaluators used during adversarial training employ the same underlying architecture. Table 2a shows the results when anonymizing in-distribution images $\sim p_{\text{test}}(x, \mathbb{N}_6)$. Examining the results based on a target classifier’s pre-processor, our approach has the highest TSR and USR in 5/6 and 4/6 cases,

³ Recall that all anonymization methods are trained on $(x, y) \sim q_{\text{data}}(x, \mathbb{N}_6)$.

Table 2. TSR (USR) in the *same architecture complete overlap* setting when anonymizing (a) in-distribution images and (b) out-of-distribution images

(a)

Attack	Preprocessor						Mean
	RGB	RGB+FD	FD	WW	CC	HP	
MISL	21.8 (60.0)	42.6 (79.2)	65.3 (87.9)	49.3 (83.1)	80.1 (85.5)	52.7 (86.7)	52.0 (80.4)
SpoC	64.8 (81.0)	94.4 (95.4)	84.3 (92.6)	90.8 (94.0)	75.4 (78.9)	83.5 (94.4)	82.2 (89.4)
Cama	91.2 (96.3)	86.8 (87.7)	94.2 (97.4)	97.3 (98.0)	88.1 (88.6)	89.7 (92.6)	91.2 (93.4)

(b)

Attack	Preprocessor						Mean
	RGB	RGB+FD	FD	WW	CC	HP	
MISL	29.2	46.4	73.0	56.1	86.9	56.2	58.0
SpoC	80.1	97.4	90.7	96.6	91.9	92.9	91.6
Cama	98.5	97.7	94.2	98.1	98.8	97.8	97.5

Table 3. TSR (USR) in the *same architecture partial overlap* setting when anonymizing (a) in-distribution images and (b) out-of-distribution images

(a)

Attack	Preprocessor						Mean
	RGB	RGB+FD	FD	WW	CC	HP	
MISL	17.7 (70.5)	12.5 (88.4)	47.4 (90.5)	26.2 (93.4)	20.9 (90.4)	35.4 (91.6)	26.7 (87.5)
SpoC	60.9 (80.6)	79.6 (90.9)	83.0 (96.0)	80.4 (96.0)	49.0 (86.4)	47.6 (89.5)	66.8 (89.9)
Cama	81.8 (91.3)	80.7 (85.3)	94.9 (98.3)	94.4 (97.1)	82.0 (93.5)	82.5 (95.3)	86.0 (93.5)

(b)

Attack	Preprocessor						Mean
	RGB	RGB+FD	FD	WW	CC	HP	
MISL	16.9 (86.6)	15.4 (81.3)	57.8 (91.4)	30.9 (85.7)	21.1 (84.0)	40.9 (92.9)	30.5 (87.0)
SpoC	70.6 (92.2)	89.9 (95.1)	88.6 (95.6)	89.1 (96.0)	61.8 (90.6)	53.7 (86.9)	75.6 (92.7)
Cama	86.6 (95.0)	96.5 (98.2)	95.5 (98.8)	95.6 (99.1)	83.6 (95.5)	92.1 (97.0)	91.7 (97.3)

respectively. Table 2b shows that our approach has the highest TSR in all cases when anonymizing out-of-distribution images $\sim p_{\text{test}}(x, \mathbb{N}_{12} \setminus \mathbb{N}_6)$.⁴

Same Architecture Partial Overlap. In this setting, an attack method is unaware of all possible classes of image learned by target classifiers F , which are trained over $(x, y) \sim p_{\text{data}}(x, \mathbb{N}_{12})$. This represents a slightly more realistic scenario. Table 3a shows the results when anonymizing in-distribution images. We achieve the highest TSR and USR in 6/6 and 5/6 cases, respectively. W.r.t. anonymizing out-of-distribution, Table 3b shows that Cama achieves the highest TSR and USR in all cases.

⁴ Note that $\mathbb{N}_{12} \setminus \mathbb{N}_6 = \{7, \dots, 12\}$.

Table 4. TSR (USR) in the *architecture transfer complete overlap* setting when anonymizing (a) in-distribution images and (b) out-of-distribution images

(a)

		Preprocessor						
Attack		RGB	RGB+FD	FD	WW	CC	HP	Mean
R-50	MISL	20.8 (57.2)	20.8 (76.0)	71.3 (89.6)	55.1 (86.4)	45.5 (67.8)	69.7 (90.6)	47.2 (77.9)
	SpoC	60.0 (75.6)	78.7 (91.6)	90.5 (94.5)	88.1 (91.6)	73.1 (81.0)	77.2 (89.3)	77.9 (87.3)
	Cama	87.9 (92.3)	79.8 (83.7)	92.0 (92.5)	95.1 (95.9)	93.9 (95.9)	89.3 (89.9)	89.7 (91.7)
D-100	MISL	28.7 (59.1)	57.4 (75.4)	62.0 (86.8)	54.9 (83.6)	96.8 (99.0)	62.9 (88.7)	60.4 (82.1)
	SpoC	62.0 (77.0)	86.9 (91.5)	88.7 (94.2)	86.1 (92.9)	78.9 (88.5)	87.0 (95.9)	81.6 (90.0)
	Cama	97.8 (98.7)	97.4 (97.8)	98.8 (99.3)	99.5 (99.8)	98.6 (98.9)	96.9 (99.5)	98.2 (99.0)
V-16	MISL	16.6 (83.2)	60.8 (84.3)	50.3 (83.9)	42.0 (83.7)	56.8 (77.8)	66.2 (86.2)	48.8 (83.2)
	SpoC	46.0 (80.1)	95.5 (96.8)	90.3 (95.3)	69.6 (88.0)	89.2 (93.3)	84.5 (91.3)	79.2 (90.8)
	Cama	88.0 (95.9)	99.0 (99.3)	98.1 (98.8)	87.4 (96.0)	98.7 (99.3)	98.4 (98.8)	94.9 (98.1)

(b)

		Preprocessor						
Attack		RGB	RGB+FD	FD	WW	CC	HP	Mean
R-50	MISL	30.3	27.8	77.1	64.9	51.4	74.8	54.4
	SpoC	75.2	83.8	95.5	96.6	87.7	86.7	87.6
	Cama	95.9	96.7	99.2	99.4	98.9	99.1	98.2
D-100	MISL	34.9	73.3	67.6	61.4	97.5	66.9	66.9
	SpoC	80.9	93.6	94.2	90.9	84.4	92.5	89.4
	Cama	99.1	99.6	99.6	99.7	99.3	98.6	99.3
V-16	MISL	17.1	71.9	50.6	50.8	68.3	71.6	55.0
	SpoC	55.8	98.2	92.3	77.4	96.3	93.8	85.6
	Cama	91.6	99.8	98.2	91.7	99.3	99.3	96.6

Architecture Transfer Complete Overlap. To investigate whether the attacks transfer to other architectures—i.e. architectures that are distinct from an attack method’s ResNet-18-based evaluator—we ran experiments using different target classifier architectures: ResNet-50 (R-50), DenseNet-100 (D-100) and VGG-16 (V-16). Table 4a shows the results when anonymizing in-distribution images: the success rates and trend are similar to what we observed when attacking ResNet-18 target classifiers (Table 2b). In particular, Cama has the highest TSR and USR in 18/18 and 14/18 cases, respectively. On out-of-distribution images, we attain the highest success rate in all cases (Table 4b).

Architecture Transfer Partial Overlap. This represents the most realistic and interesting setting for assessing the performance of a non-interactive black-box attack. Notably, on in-distribution images we achieve the highest TSR and USR in 18/18 and 15/18 cases (Table 5a), respectively. Moreover, as shown in Table 5b, we attain the best success rates in every case when anonymizing out-of-distribution images.

4.3 Discussion

The experimental results validate that our approach (Cama) is able to reliably perform targeted transformations. Importantly, not only can we successfully

Table 5. TSR (USR) in the *architecture transfer partial overlap* setting when anonymizing (a) in-distribution images and (b) out-of-distribution images

(a)

		Preprocessor						
Attack		RGB	RGB+FD	FD	WW	CC	HP	Mean
R-50	MISL	8.4 (81.5)	8.2 (89.5)	20.8 (91.7)	19.1 (96.2)	33.8 (83.0)	36.5 (91.6)	21.1 (88.9)
	SpoC	62.7 (90.3)	66.4 (95.7)	73.9 (95.0)	71.2 (96.6)	70.9 (94.7)	51.2 (91.6)	66.0 (94.0)
	CamA	92.6 (97.6)	73.3 (88.2)	83.3 (98.2)	91.9 (99.3)	81.9 (96.4)	75.3 (88.4)	83.0 (94.7)
D-100	MISL	11.5 (71.9)	31.0 (91.8)	37.6 (96.9)	20.6 (94.7)	16.2 (93.1)	24.1 (98.3)	23.5 (91.1)
	SpoC	52.6 (81.9)	89.2 (96.2)	85.9 (97.5)	79.8 (94.5)	76.3 (96.5)	60.9 (94.5)	74.1 (93.5)
	CamA	88.3 (95.0)	96.7 (98.6)	96.3 (99.5)	96.9 (99.2)	88.9 (97.4)	88.9 (99.2)	92.7 (98.2)
V-16	MISL	30.1 (86.5)	21.5 (96.2)	46.6 (85.8)	27.5 (97.2)	96.9 (99.9)	28.6 (96.4)	41.9 (93.7)
	SpoC	81.7 (93.3)	81.7 (96.3)	76.3 (92.4)	80.5 (95.1)	64.1 (90.6)	61.3 (96.2)	74.3 (94.0)
	CamA	98.3 (99.5)	95.1 (98.4)	94.5 (99.0)	94.3 (99.4)	97.3 (98.9)	92.9 (99.2)	95.4 (99.1)

(b)

		Preprocessor						
Attack		RGB	RGB+FD	FD	WW	CC	HP	Mean
R-50	MISL	7.6 (79.3)	9.8 (85.9)	27.1 (82.2)	22.8 (85.4)	39.2 (86.0)	42.0 (91.9)	24.8 (85.1)
	SpoC	70.7 (93.0)	77.0 (92.8)	82.8 (94.6)	80.3 (94.3)	72.5 (91.3)	56.7 (94.6)	73.3 (93.4)
	CamA	96.1 (97.9)	88.4 (94.4)	88.7 (96.0)	97.5 (99.1)	81.3 (93.6)	86.8 (97.1)	89.8 (96.4)
D-100	MISL	10.6 (78.4)	34.7 (85.5)	40.5 (82.9)	20.7 (85.6)	15.1 (80.0)	29.4 (86.9)	25.2 (83.2)
	SpoC	66.5 (89.7)	93.4 (97.0)	91.1 (96.5)	86.9 (96.2)	82.1 (91.3)	75.5 (94.2)	82.6 (94.1)
	CamA	92.3 (95.5)	97.8 (98.5)	95.2 (98.3)	97.3 (98.8)	91.2 (95.6)	94.7 (98.0)	94.8 (97.4)
V-16	MISL	33.9 (87.7)	31.4 (84.6)	49.8 (88.0)	23.9 (83.6)	98.0 (99.6)	30.6 (83.2)	44.6 (87.8)
	SpoC	77.7 (95.7)	85.8 (94.9)	79.0 (92.0)	84.9 (94.8)	74.1 (90.6)	70.0 (87.0)	78.6 (92.5)
	CamA	98.9 (99.6)	97.6 (98.8)	93.0 (97.4)	95.4 (97.5)	96.4 (98.8)	95.9 (97.9)	96.2 (98.3)

perform targeted transformations on in-distribution images captured by camera models *known* to our framework, but also on out-of-distribution images captured by camera models *unknown* to our framework. Most significantly, our attack methodology transfers across different target classifiers, i.e. as we vary a target classifier’s architecture, preprocessing module and training data. Our results are non-trivial: for instance, there is no reason that the feature space of a VGG-16-based target classifier should *behave* in the same manner as an adversarial evaluator’s ResNet-18. This shows that our method has good generalization ability and that the applied transformations go above and beyond mere adversarial noise. This last point is especially apparent when one considers the results attained using adversarial example methods (Appendix C).

As hypothesized, it is critical to transform both high and low spatial frequency artifacts. This can be readily seen by the poor performance of MISL, which wholly focuses on the transformation of high-frequency artifacts, and therefore cannot attend to lower-frequency model-specific artifacts used by RGB-based target classifiers (i.e. without image content suppression). Moreover, while the method of prediction-error filtering, using a constrained convolutional layer, has been successfully used for camera model attribution, it was originally proposed for image manipulation detection [3]. It is unclear how these features relate to model-specific artifacts extracted by other methods that suppress image content as a preprocessing step, i.e. other than being useful for image manipulation detection.

Principally, when employed by an evaluator (as is the case for MISL), the learned generator is incapable of reliably causing targeted misclassifications when faced by target classifiers that employ a dissimilar image content suppressor and/or architecture.

During optimization, the generator of SpoC is guided by an evaluator and discriminator that concatenate an RGB input image channel-wise with its image residual. We posit that concatenating these input modalities does not effectively force the generative model to update its parameters s.t. lower-frequency artifacts contained in the RGB channels of an input are attended to. As evidenced by the results, the evaluator and discriminator of SpoC pay more attention to the image residual channels. In contradistinction to SpoC, Cama *constrains* its generator using a dual-stream evaluator that independently reasons over high and low spatial frequency artifacts. This consistently improves performance, since the generator is tasked with fooling both streams such that it cannot easily take a *shortcut*—i.e. predominantly focus on the salient high-frequency information. Patently, anonymization methods that are capable of transforming model-specific artifacts of a high and low spatial frequency are better able to deceive unknown non-interactive black-box target classifiers of varying types. This is particularly useful, since we do not know *a priori* in which space a target classifier operates.

5 Conclusion

The method proposed in this paper, Cama, offers a way to preserve privacy by transforming an image’s ground truth camera model-specific artifacts to those of a disparate target camera model. By formulating the learning procedure as necessitating the transformation of both high and low spatial frequency artifacts, we proposed to incorporate a fixed pre-trained dual-stream evaluator into the generative objective. The evaluator serves to reinforce the transformation process by *independently* reasoning over information present in the high and low spatial frequencies. Experimental results demonstrate that our approach (i) can successfully anonymize images captured by camera models *known* and *unknown* to our framework, and (ii) results in targeted transformations that are non-interactive black-box target classifier-agnostic (i.e. as we vary the architecture, training data and preprocessing module of a target classifier).

While the preservation of privacy is evidently beneficial to certain vulnerable individuals, anonymization could equally be open to misuse [18]. As society is at present afflicted by the deliberate dissemination of misinformation, we require more robust and reliable digital forensic methods for authenticating the origin and integrity of images. In particular, when faced by synthesized photo-realistic *deepfakes* [12], which additionally mimic the intrinsic artifacts of a target camera model (and/or device) as made possible by Cama.

Acknowledgments. JTAA is supported by the Royal Academy of Engineering (RAEng) and the Office of the Chief Science Adviser for National Security under the UK Intelligence Community Postdoctoral Fellowship Programme.

References

1. Arandjelović, R., Zisserman, A.: Object discovery with a copy-pasting gan. arXiv preprint arXiv:1905.11369 (2019)
2. Barni, M., Kallas, K., Nowroozi, E., Tondi, B.: On the transferability of adversarial examples against cnn-based image forensics. In: ICASSP 2019-2019 IEEE International Conference on Acoustics, Speech and Signal Processing (ICASSP). pp. 8286–8290. IEEE (2019)
3. Bayar, B., Stamm, M.C.: A deep learning approach to universal image manipulation detection using a new convolutional layer. In: Proceedings of the 4th ACM Workshop on Information Hiding and Multimedia Security. pp. 5–10. ACM (2016)
4. Bayar, B., Stamm, M.C.: Design principles of convolutional neural networks for multimedia forensics. *Electronic Imaging* **2017**(7), 77–86 (2017)
5. Bayar, B., Stamm, M.C.: Towards open set camera model identification using a deep learning framework. In: 2018 IEEE International Conference on Acoustics, Speech and Signal Processing (ICASSP). pp. 2007–2011. IEEE (2018)
6. Bayram, S., Sencar, H., Memon, N., Avcibas, I.: Source camera identification based on cfa interpolation. In: IEEE International Conference on Image Processing 2005. vol. 3, pp. III–69. IEEE (2005)
7. Blau, Y., Michaeli, T.: The perception-distortion tradeoff. In: Proceedings of the IEEE Conference on Computer Vision and Pattern Recognition. pp. 6228–6237 (2018)
8. Böhme, R., Kirchner, M.: Counter-forensics: Attacking image forensics. In: Digital image forensics, pp. 327–366. Springer (2013)
9. Bondi, L., Baroffio, L., Güera, D., Bestagini, P., Delp, E.J., Tubaro, S.: First steps toward camera model identification with convolutional neural networks. *IEEE Signal Processing Letters* **24**(3), 259–263 (2016)
10. Bonettini, N., Bondi, L., Güera, D., Mandelli, S., Bestagini, P., Tubaro, S., Delp, E.J.: Fooling prnu-based detectors through convolutional neural networks. In: 2018 26th European Signal Processing Conference (EUSIPCO). pp. 957–961. IEEE (2018)
11. Bonettini, N., Güera, D., Bondi, L., Bestagini, P., Delp, E.J., Tubaro, S.: Image anonymization detection with deep handcrafted features. In: 2019 IEEE International Conference on Image Processing (ICIP). pp. 2304–2308. IEEE (2019)
12. Caldwell, M., Andrews, J., Tanay, T., Griffin, L.: Ai-enabled future crime. *Crime Science* **9**(1), 1–13 (2020)
13. Chen, C., Stamm, M.C.: Camera model identification framework using an ensemble of demosaicing features. In: 2015 IEEE International Workshop on Information Forensics and Security (WIFS). pp. 1–6. IEEE (2015)
14. Chen, C., Zhao, X., Stamm, M.C.: Mislgan: An anti-forensic camera model falsification framework using a generative adversarial network. In: 2018 25th IEEE International Conference on Image Processing (ICIP). pp. 535–539. IEEE (2018)
15. Chen, C., Zhao, X., Stamm, M.C.: Generative adversarial attacks against deep-learning-based camera model identification. *IEEE Transactions on Information Forensics and Security* (2019)
16. Chen, M., Fridrich, J., Goljan, M., Lukás, J.: Determining image origin and integrity using sensor noise. *IEEE Transactions on information forensics and security* **3**(1), 74–90 (2008)
17. Chen, T., Zhai, X., Ritter, M., Lucic, M., Houlsby, N.: Self-supervised gans via auxiliary rotation loss. In: Proceedings of the IEEE Conference on Computer Vision and Pattern Recognition. pp. 12154–12163 (2019)

18. Chesney, R., Citron, D.K.: Deep fakes: A looming challenge for privacy, democracy, and national security (2018)
19. Choi, K.S., Lam, E.Y., Wong, K.K.: Source camera identification by jpeg compression statistics for image forensics. In: TENCON 2006-2006 IEEE Region 10 Conference. pp. 1–4. IEEE (2006)
20. Choi, K.S., Lam, E.Y., Wong, K.K.: Source camera identification using footprints from lens aberration. In: Digital photography II. vol. 6069, pp. 172–179 (2006)
21. Cozzolino, D., Thies, J., Rössler, A., Nießner, M., Verdoliva, L.: Spoc: Spoofing camera fingerprints. arXiv preprint arXiv:1911.12069 (2019)
22. Dirik, A.E., Karaküçük, A.: Forensic use of photo response non-uniformity of imaging sensors and a counter method. *Optics express* **22**(1), 470–482 (2014)
23. Dirik, A.E., Sencar, H.T., Memon, N.: Analysis of seam-carving-based anonymization of images against prnu noise pattern-based source attribution. *IEEE Transactions on Information Forensics and Security* **9**(12), 2277–2290 (2014)
24. Entrieri, J., Kirchner, M.: Patch-based desynchronization of digital camera sensor fingerprints. *Electronic Imaging* **2016**(8), 1–9 (2016)
25. Filler, T., Fridrich, J., Goljan, M.: Using sensor pattern noise for camera model identification. In: 2008 15th IEEE International Conference on Image Processing. pp. 1296–1299. IEEE (2008)
26. Fridrich, J.: Digital image forensics. *IEEE Signal Processing Magazine* **26**(2), 26–37 (2009)
27. Fridrich, J.: Sensor defects in digital image forensic. In: Digital Image Forensics, pp. 179–218. Springer (2013)
28. Geirhos, R., Jacobsen, J.H., Michaelis, C., Zemel, R., Brendel, W., Bethge, M., Wichmann, F.A.: Shortcut learning in deep neural networks. arXiv preprint arXiv:2004.07780 (2020)
29. Geradts, Z.J., Bijhold, J., Kieft, M., Kurosawa, K., Kuroki, K., Saitoh, N.: Methods for identification of images acquired with digital cameras. In: Enabling technologies for law enforcement and security. vol. 4232, pp. 505–512. International Society for Optics and Photonics (2001)
30. Gloe, T.: Feature-based forensic camera model identification. In: Transactions on data hiding and multimedia security VIII, pp. 42–62. Springer (2012)
31. Gloe, T., Böhme, R.: The ‘dresden image database’ for benchmarking digital image forensics. In: Proceedings of the 2010 ACM Symposium on Applied Computing. pp. 1584–1590. ACM (2010)
32. Gloe, T., Kirchner, M., Winkler, A., Böhme, R.: Can we trust digital image forensics? In: Proceedings of the 15th ACM international conference on Multimedia. pp. 78–86. ACM (2007)
33. Goodfellow, I., Pouget-Abadie, J., Mirza, M., Xu, B., Warde-Farley, D., Ozair, S., Courville, A., Bengio, Y.: Generative adversarial nets. In: Advances in neural information processing systems. pp. 2672–2680 (2014)
34. Goodfellow, I.J., Shlens, J., Szegedy, C.: Explaining and harnessing adversarial examples. arXiv preprint arXiv:1412.6572 (2014)
35. Gragnaniello, D., Marra, F., Poggi, G., Verdoliva, L.: Analysis of adversarial attacks against cnn-based image forgery detectors. In: 2018 26th European Signal Processing Conference (EUSIPCO). pp. 967–971. IEEE (2018)
36. Güera, D., Wang, Y., Bondi, L., Bestagini, P., Tubaro, S., Delp, E.J.: A counter-forensic method for cnn-based camera model identification. In: Proceedings of the IEEE Conference on Computer Vision and Pattern Recognition Workshops. pp. 28–35 (2017)

37. He, K., Zhang, X., Ren, S., Sun, J.: Deep residual learning for image recognition. In: Proceedings of the IEEE conference on computer vision and pattern recognition. pp. 770–778 (2016)
38. Holst, G.C.: Ccd arrays, cameras, and displays (1998)
39. Huang, G., Liu, Z., Van Der Maaten, L., Weinberger, K.Q.: Densely connected convolutional networks. In: Proceedings of the IEEE conference on computer vision and pattern recognition. pp. 4700–4708 (2017)
40. Isola, P., Zhu, J.Y., Zhou, T., Efros, A.A.: Image-to-image translation with conditional adversarial networks. In: Proceedings of the IEEE conference on computer vision and pattern recognition. pp. 1125–1134 (2017)
41. Johnson, J., Alahi, A., Fei-Fei, L.: Perceptual losses for real-time style transfer and super-resolution. In: European conference on computer vision. pp. 694–711. Springer (2016)
42. Karaküçük, A., Dirik, A.E.: Adaptive photo-response non-uniformity noise removal against image source attribution. *Digital Investigation* **12**, 66–76 (2015)
43. Karras, T., Aila, T., Laine, S., Lehtinen, J.: Progressive growing of gans for improved quality, stability, and variation. *arXiv preprint arXiv:1710.10196* (2017)
44. Kharrazi, M., Sencar, H.T., Memon, N.: Blind source camera identification. In: 2004 International Conference on Image Processing, 2004. ICIP'04. vol. 1, pp. 709–712. IEEE (2004)
45. Kingma, D.P., Ba, J.: Adam: A method for stochastic optimization. *arXiv preprint arXiv:1412.6980* (2014)
46. Kirchner, M., Gloe, T.: Forensic camera model identification. *Handbook of Digital Forensics of Multimedia Data and Devices* pp. 329–374 (2015)
47. Kuzin, A., Fattakhov, A., Kibardin, I., Iglovikov, V.I., Dautov, R.: Camera model identification using convolutional neural networks. In: 2018 IEEE International Conference on Big Data (Big Data). pp. 3107–3110. IEEE (2018)
48. Lukáš, J., Fridrich, J., Goljan, M.: Detecting digital image forgeries using sensor pattern noise. In: Security, Steganography, and Watermarking of Multimedia Contents VIII. vol. 6072, p. 60720Y. International Society for Optics and Photonics (2006)
49. Lukáš, J., Fridrich, J., Goljan, M.: Digital camera identification from sensor pattern noise. *IEEE Transactions on Information Forensics and Security* **1**(2), 205–214 (2006)
50. Madry, A., Makelov, A., Schmidt, L., Tsipras, D., Vladu, A.: Towards deep learning models resistant to adversarial attacks. *arXiv preprint arXiv:1706.06083* (2017)
51. Mandelli, S., Bondi, L., Lameri, S., Lipari, V., Bestagini, P., Tubaro, S.: Inpainting-based camera anonymization. In: 2017 IEEE International Conference on Image Processing (ICIP). pp. 1522–1526. IEEE (2017)
52. Mao, X., Li, Q., Xie, H., Lau, R.Y., Wang, Z., Paul Smolley, S.: Least squares generative adversarial networks. In: Proceedings of the IEEE International Conference on Computer Vision. pp. 2794–2802 (2017)
53. Marra, F., Gragnaniello, D., Verdoliva, L.: On the vulnerability of deep learning to adversarial attacks for camera model identification. *Signal Processing: Image Communication* **65**, 240–248 (2018)
54. Marra, F., Poggi, G., Sansone, C., Verdoliva, L.: Evaluation of residual-based local features for camera model identification. In: International Conference on Image Analysis and Processing. pp. 11–18. Springer (2015)
55. Marra, F., Poggi, G., Sansone, C., Verdoliva, L.: A study of co-occurrence based local features for camera model identification. *Multimedia Tools and Applications* **76**(4), 4765–4781 (2017)

56. Mathieu, M.F., Zhao, J.J., Zhao, J., Ramesh, A., Sprechmann, P., LeCun, Y.: Disentangling factors of variation in deep representation using adversarial training. In: *Advances in Neural Information Processing Systems*. pp. 5040–5048 (2016)
57. Mirza, M., Osindero, S.: Conditional generative adversarial nets. arXiv preprint arXiv:1411.1784 (2014)
58. Perarnau, G., Van De Weijer, J., Raducanu, B., Álvarez, J.M.: Invertible conditional gans for image editing. arXiv preprint arXiv:1611.06355 (2016)
59. Reed, S., Akata, Z., Yan, X., Logeswaran, L., Schiele, B., Lee, H.: Generative adversarial text to image synthesis. arXiv preprint arXiv:1605.05396 (2016)
60. Rony, J., Hafemann, L.G., Oliveira, L.S., Ayed, I.B., Sabourin, R., Granger, E.: Decoupling direction and norm for efficient gradient-based l2 adversarial attacks and defenses. In: *Proceedings of the IEEE Conference on Computer Vision and Pattern Recognition*. pp. 4322–4330 (2019)
61. Simonyan, K., Zisserman, A.: Very deep convolutional networks for large-scale image recognition. arXiv preprint arXiv:1409.1556 (2014)
62. Society, I.S.P.: IEEE Signal Processing Cup 2018: Forensic Camera Model Identification Challenge (2018), <https://www.kaggle.com/c/sp-society-camera-model-identification>
63. Szegedy, C., Zaremba, W., Sutskever, I., Bruna, J., Erhan, D., Goodfellow, I., Fergus, R.: Intriguing properties of neural networks. arXiv preprint arXiv:1312.6199 (2013)
64. Tuama, A., Comby, F., Chaumont, M.: Source camera model identification using features from contaminated sensor noise. In: *International Workshop on Digital Watermarking*. pp. 83–93. Springer (2015)
65. Tuama, A., Comby, F., Chaumont, M.: Camera model identification with the use of deep convolutional neural networks. In: *2016 IEEE International workshop on information forensics and security (WIFS)*. pp. 1–6. IEEE (2016)
66. Wang, Z., Tang, X., Luo, W., Gao, S.: Face aging with identity-preserved conditional generative adversarial networks. In: *Proceedings of the IEEE Conference on Computer Vision and Pattern Recognition*. pp. 7939–7947 (2018)
67. Xu, G., Shi, Y.Q.: Camera model identification using local binary patterns. In: *2012 IEEE International Conference on Multimedia and Expo*. pp. 392–397. IEEE (2012)
68. Yang, H., Huang, D., Wang, Y., Jain, A.K.: Learning face age progression: A pyramid architecture of gans. In: *Proceedings of the IEEE Conference on Computer Vision and Pattern Recognition*. pp. 31–39 (2018)
69. Zhu, J.Y., Krähenbühl, P., Shechtman, E., Efros, A.A.: Generative visual manipulation on the natural image manifold. In: *European Conference on Computer Vision*. pp. 597–613. Springer (2016)
70. Zhu, J.Y., Park, T., Isola, P., Efros, A.A.: Unpaired image-to-image translation using cycle-consistent adversarial networks. In: *Proceedings of the IEEE international conference on computer vision*. pp. 2223–2232 (2017)
71. Zhu, J.Y., Zhang, R., Pathak, D., Darrell, T., Efros, A.A., Wang, O., Shechtman, E.: Toward multimodal image-to-image translation. In: *Advances in Neural Information Processing Systems*. pp. 465–476 (2017)

A Extended Motivation

The central premise of this work is that there exist both *high* and *low* spatial frequency artifacts that constitute useful signals for standard camera model attribution (and ipso facto camera model anonymization). We now briefly provide discussion in support of this.

We denote by $x \in \mathbb{R}^d$ an observable digital image (e.g. stored as a `.jpeg` or `.tiff` file). The in-camera processing pipeline in digital cameras is complex in nature and can vary greatly between camera models. To capture the *common* elements of in-camera processing, [16] proposed the following simplified imaging sensor output model (prior to color interpolation):

$$x = g^\gamma [(1 + \mathcal{Y})u + \Lambda]^\gamma + \Theta_q \quad (6)$$

$$= (gu)^\gamma [1 + (\mathcal{Y} + \Lambda/u)]^\gamma + \Theta_q, \quad (7)$$

where u is the incident light intensity, g is the color channel gain, γ is the gamma correction, \mathcal{Y} is the device-specific zero-mean noise-like factor responsible for photo-response non-uniformity, Θ_q is the quantization noise and Λ is a combination of all other noise sources. Retaining only the first two terms of the Taylor expansion of $[1 + (\mathcal{Y} + \Lambda/u)]^\gamma$ at $\mathcal{Y} + \Lambda/u = 0$, Eq. (7) becomes:

$$x \approx (gu)^\gamma (1 + \gamma\mathcal{Y} + \gamma\Lambda/u) + \Theta_q \quad (8)$$

$$= x_0 + x_0\Omega + \Theta, \quad (9)$$

where $x_0 = (gu)^\gamma$ is the image content (ideal noise-free sensor response), $\Omega = \gamma\mathcal{Y}$ is the gamma corrected photo-response non-uniformity factor and $\Theta = \gamma x_0 \Lambda/u + \Theta_q$ is a combination of random independent noise sources.

To improve the signal-to-noise between the photo-response non-uniformity signal $x_0\Omega$ and the observable image x , the image content x_0 is suppressed via a denoising filter $H : x \mapsto \hat{x}_0$:

$$x_H = x - H(x) \quad (10)$$

$$= x_0 + x_0\Omega + \Theta - \hat{x}_0 \quad (11)$$

$$= (x_0 - \hat{x}_0) + (x_0 - x)\Omega + x\Omega + \Theta \quad (12)$$

$$= x\Omega + \Xi, \quad (13)$$

where $\Xi = \Theta + (x_0 - \hat{x}_0) + (x_0 - x)\Omega$. Working with the high-frequency noise residual x_H , it is easier to estimate (and detect) Ω , because the image content has been significantly suppressed. Appositely, the unique device-specific factor Ω is commonly employed for model attribution [64,54,25,30,65,4], since it also contains non-unique artifacts (unless corrected for).

As aforementioned (Section 1), subsequent to the imaging sensor, the effects of Ω propagate nonlinearly through the in-camera processing steps that result in an observable image x and thus end up also depending on model-specific aspects, such as color interpolation, on-sensor signal transfer, sensor design and compression. Therefore, x_H contains model-specific artifacts with high spatial

frequency, i.e. *features* that change considerably in intensity over short spatial distances. However, due to denoising, $x\Omega$ in Eq. (13) no longer corresponds to the photo-response non-uniformity signal, but instead the pixel non-uniformity signal (Fig. 2). The attenuation of the image content, through denoising, results in the removal of the low spatial frequency components inherent to photo-response non-uniformity that, for instance, stem from the model-specific camera optics. Therefore, anonymizing x based on the information contained in x_H precludes the anonymization of discriminative low spatial frequency artifacts contained in $x_L = x - x_H$. Remarkably, this crucial point has been overlooked by previous model anonymization works.

B Extended Qualitative Results

In this section, we provide additional figures showing the ability of Cama to transform in-distribution (Fig. 5) and out-of-distribution (Fig. 6) input images using different target label conditions.

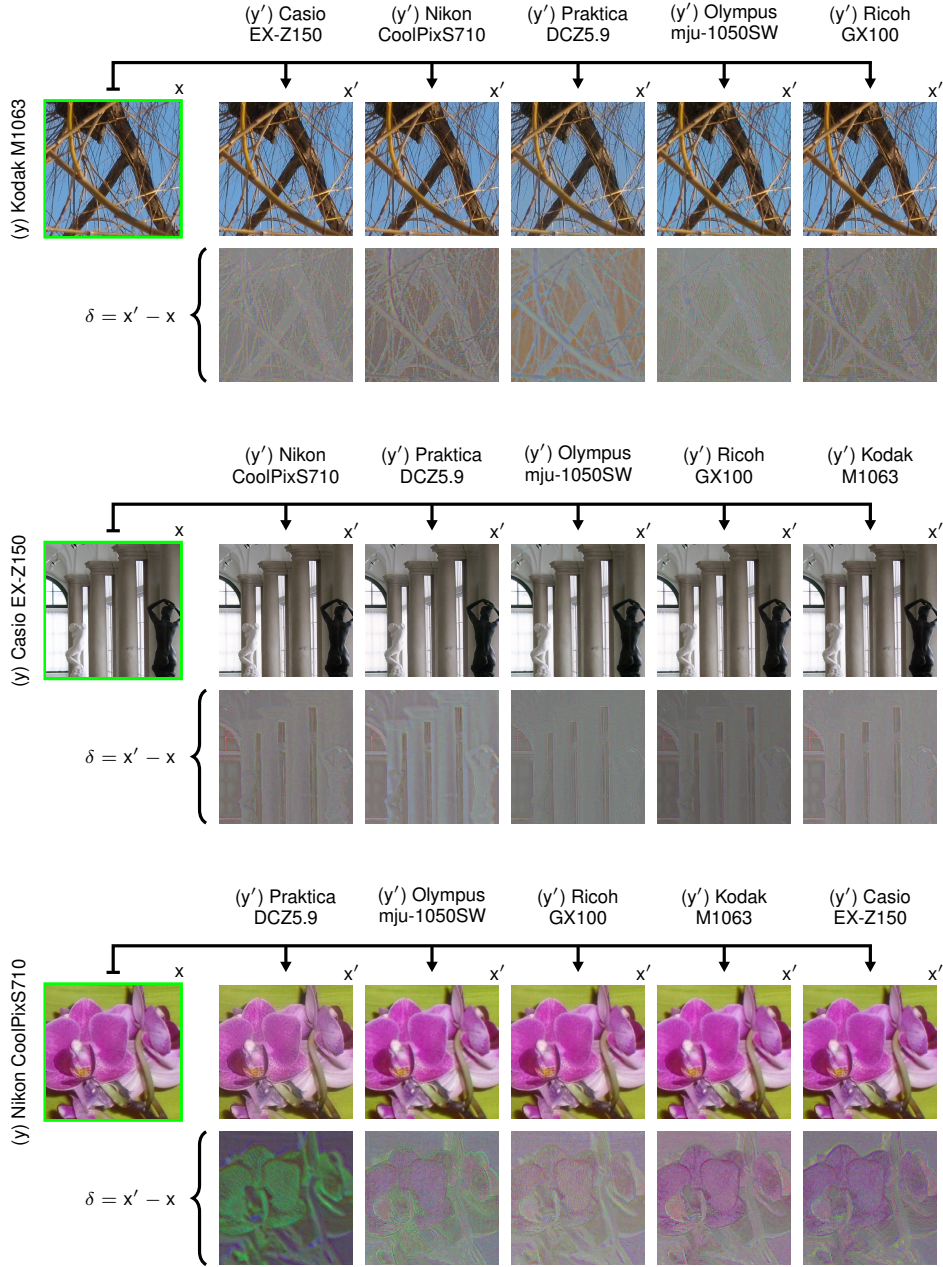


Fig. 5. Example of Cama transformed images x' with different target label conditions y' given an in-distribution input image x . The applied transformations (amplified for visualization purposes) are shown as δ . (Figure continues)

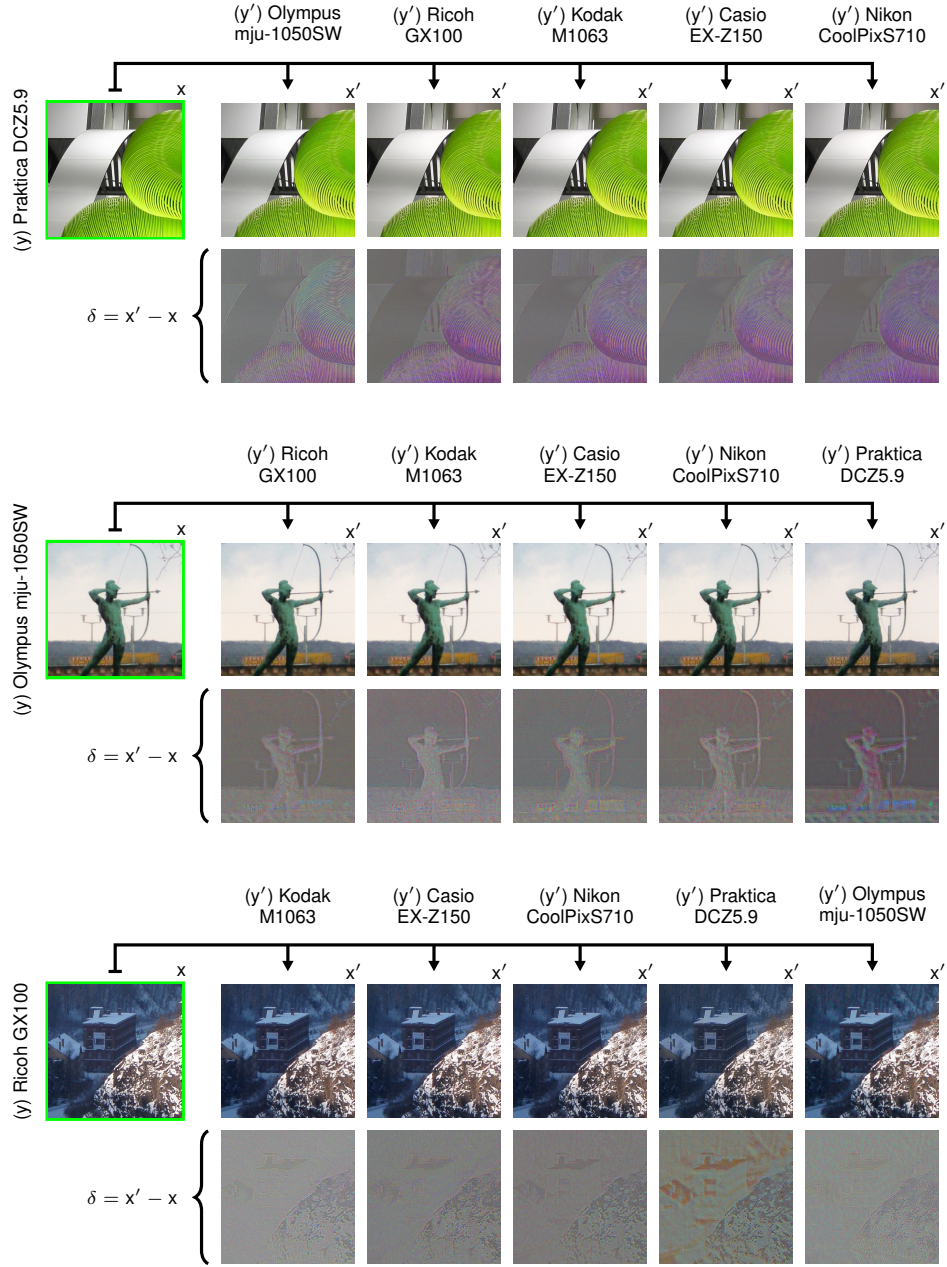


Fig. 5. (Continued). Example of Cama transformed images x' with different target label conditions y' given an in-distribution input image x . The applied transformations (amplified for visualization purposes) are shown as δ

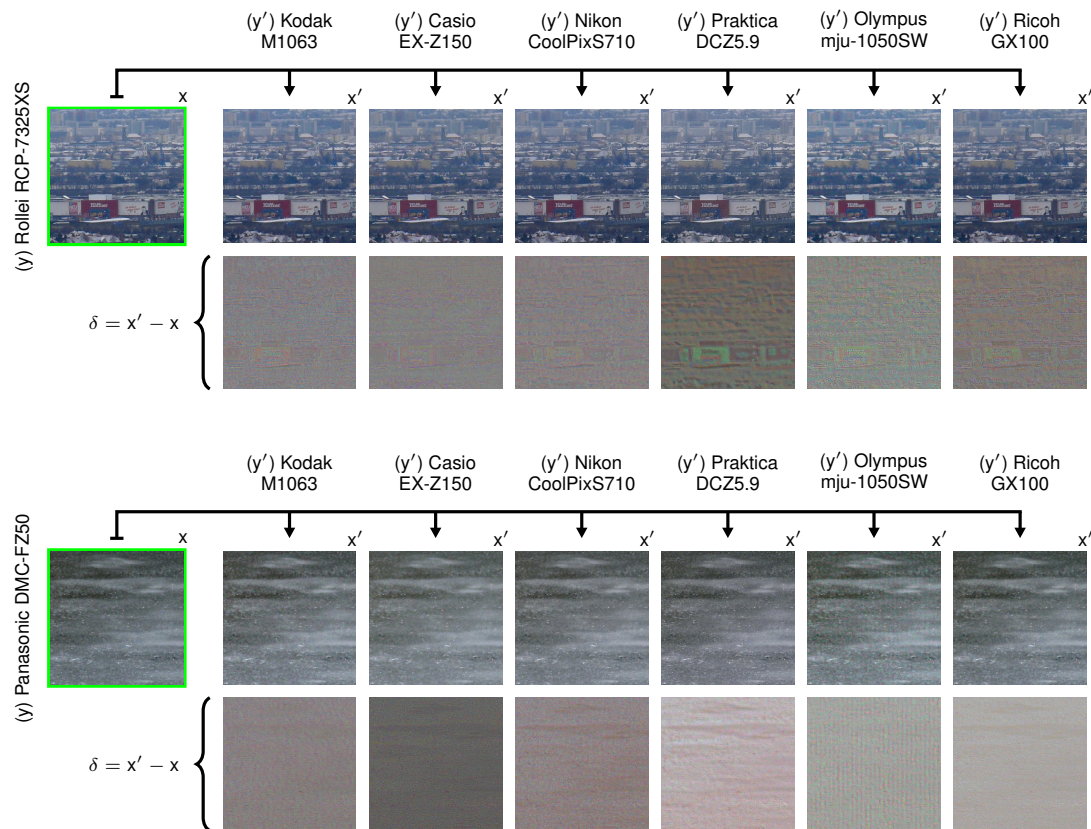


Fig. 6. Example of Cama transformed images x' with different target label conditions y' given an out-of-distribution input image x . The applied transformations (amplified for visualization purposes) are shown as δ . (Figure continues)

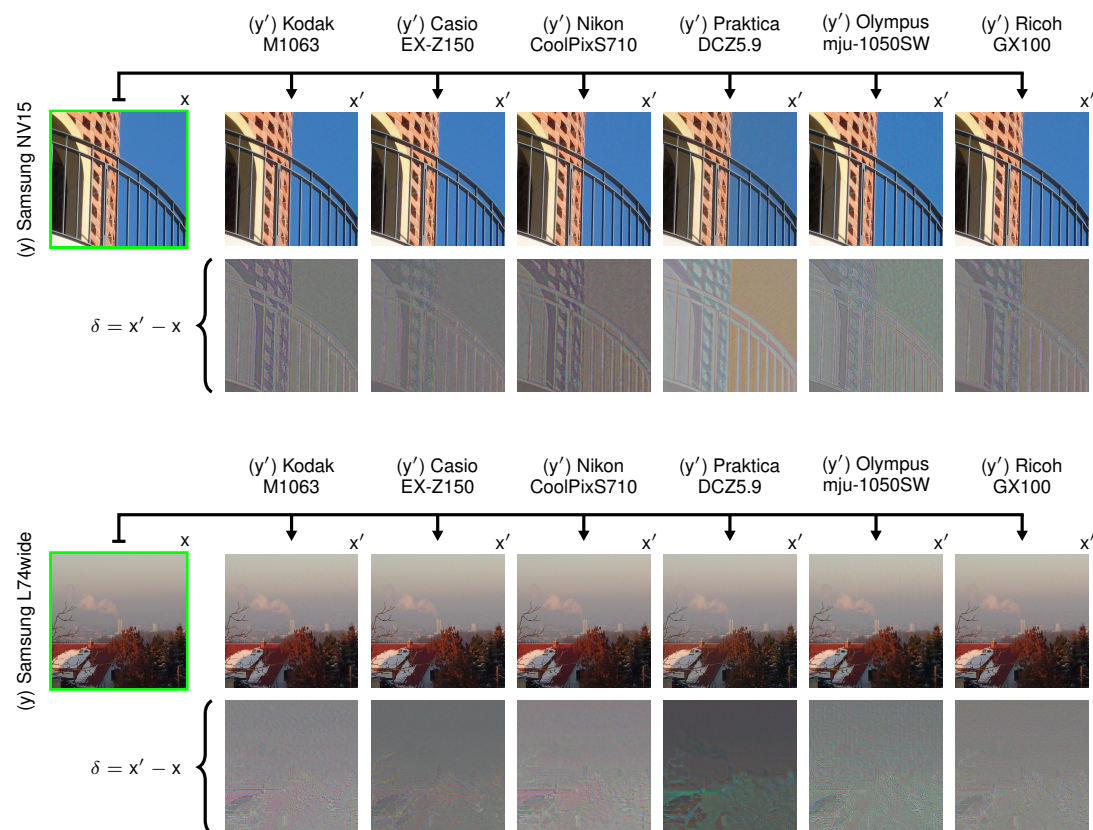


Fig. 6. (Continued). Example of Cama transformed images x' with different target label conditions y' given an out-of-distribution input image x . The applied transformations (amplified for visualization purposes) are shown as δ . (Figure continues)

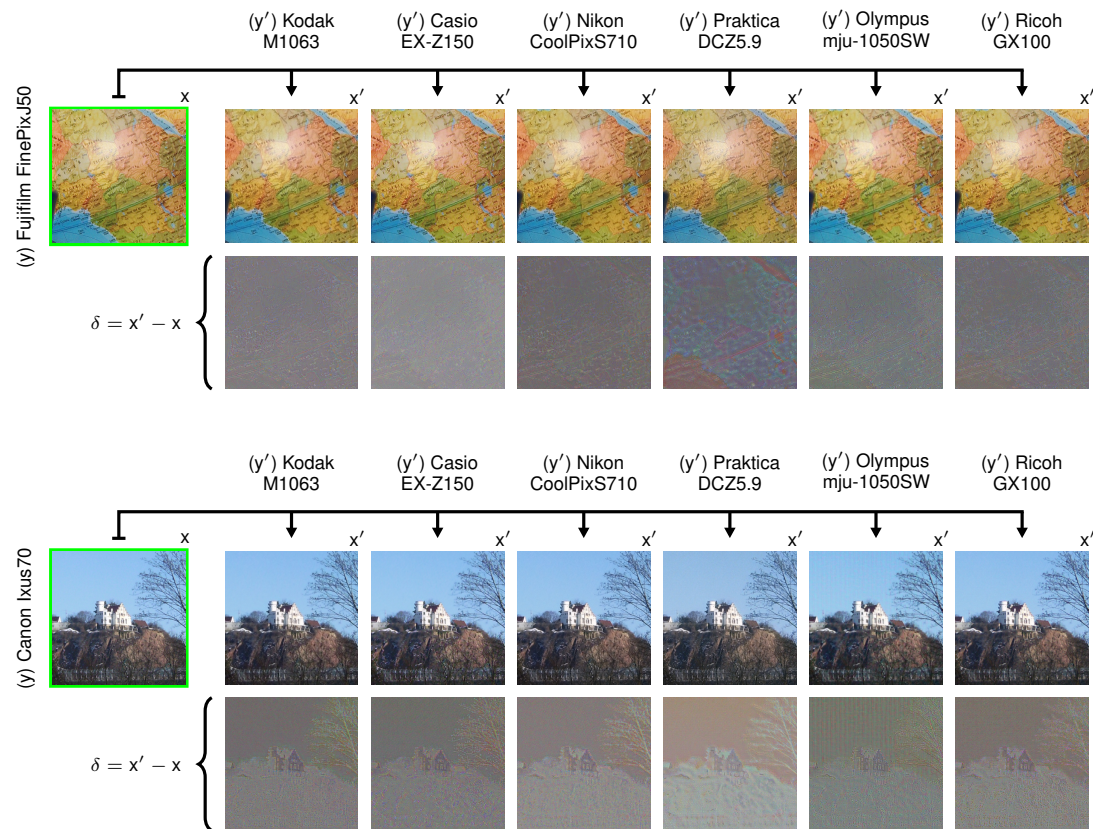


Fig. 6. (Continued). Example of Cama transformed images x' with different target label conditions y' given an out-of-distribution input image x . The applied transformations (amplified for visualization purposes) are shown as δ

C Extended Quantitative Results

From the adversarial examples literature, we perform targeted attacks using the following representative approaches: fast gradient sign method (FGSM) [34], projected gradient descent (PGD) [50] and decoupled direction and norm (DDN) [60], where the perturbations are constructed using an evaluator E with a ResNet-18 backbone architecture. (See individual descriptions below). Note that we tested several different preprocessing modules, i.e. with and without image content suppression, however results remained roughly commensurate. We therefore utilized the dual-stream evaluator of our approach (as outlined in Section 2).

To ensure a fair comparison, we set the parameters for each method s.t. the peak signal-to-noise ratio is approximately 35dB, except for DDN. DDN is designed to efficiently find small perturbations that fool a proxy model. Table 6 shows the mean peak signal-to-noise ratio when anonymizing in-distribution images and out-of-distribution images $\sim p_{\text{test}}$, whereas Tables 7a, 7b, 8a, 8b, 9a, 9b, 10a and 10b (below) show the targeted and untargeted success rates of these attack methods in comparison to our approach Cama.

FGSM. For an L^∞ -bounded adversary, the one-step FGSM computes a targeted adversarial example as:

$$x' = x - \epsilon \operatorname{sgn}(-\nabla_x \log E(x)_{y'}), \quad (14)$$

where ϵ is the magnitude of the perturbation.

PGD. PGD is an iterative variant of FGSM. At iteration $t + 1$, PGD follows the update rule:

$$x'_{t+1} = \operatorname{proj}(x'_t - \alpha \operatorname{sgn}(-\nabla_x \log E(x'_t)_{y'})), \quad (15)$$

where α is the step size and proj is a projection into the L^∞ -ball with radius ϵ and center x .

DDN. For an L^2 -bounded adversary, DDN is an iterative method (similar to PGD) that induces a targeted misclassification with low L^2 norm. At iteration $t + 1$, DDN follows the update rule:

$$x'_{t+1} = \operatorname{proj}\left(x'_t - \alpha \frac{-\nabla_x \log E(x'_t)_{y'}}{\|-\nabla_x \log E(x'_t)_{y'}\|_2}\right), \quad (16)$$

where α is the step size and proj is a projection into the ℓ_2 -ball with radius ϵ_{t+1} and center x . The radius is adapted based on the current distortion s.t. if x'_t is an adversarial example then $\epsilon_{t+1} = (1-\gamma)\|x'_t - x\|_2$, otherwise $\epsilon_{t+1} = (1+\gamma)\|x'_t - x\|_2$, where γ is a factor to modify the norm in each iteration.

Table 6. Mean peak signal-to-noise ratio when anonymizing in-distribution images (and out-of-distribution images in parentheses) $\sim p_{\text{test}}$

FGSM	PGD	DDN	MISL	SpoC	Cama
35.0 (35.0)	34.6 (34.6)	69.3 (88.1)	35.2 (34.7)	35.3 (34.8)	35.7 (35.3)

Table 7. TSR (USR) in the *same architecture complete overlap* setting when anonymizing (a) in-distribution images (cf. Table 2a) and (b) out-of-distribution images (cf. Table 2b)

(a)

Attack	Preprocessor						Mean
	RGB	RGB+FD	FD	WW	CC	HP	
FGSM	15.3 (72.2)	15.6 (75.3)	12.9 (60.4)	18.7 (73.1)	16.6 (70.8)	18.3 (75.8)	16.2 (71.3)
PGD	17.9 (76.1)	14.6 (69.1)	16.0 (65.9)	58.3 (88.7)	17.0 (75.5)	16.6 (67.5)	23.4 (73.8)
DDN	0.0 (0.2)	0.0 (0.2)	0.1 (0.2)	0.0 (0.2)	0.0 (0.2)	0.1 (0.5)	0.0 (0.2)
Cama	91.2 (96.3)	86.8 (87.7)	94.2 (97.4)	97.3 (98.0)	88.1 (88.6)	89.7 (92.6)	91.2 (93.4)

(b)

Attack	Preprocessor						Mean
	RGB	RGB+FD	FD	WW	CC	HP	
FGSM	25.6	19.7	23.5	42.7	25.0	22.0	26.4
PGD	21.7	17.6	19.5	60.2	18.2	19.2	26.1
DDN	16.8	17.4	18.3	19.2	18.3	18.3	18.0
Cama	98.5	97.7	94.2	98.1	98.8	97.8	97.5

Table 8. TSR (USR) in the *same architecture partial overlap* setting when anonymizing (a) in-distribution images (cf. Table 3a) and (b) out-of-distribution images (cf. Table 3b)

(a)

Attack	Preprocessor						Mean
	RGB	RGB+FD	FD	WW	CC	HP	
FGSM	10.7 (86.6)	0.5 (94.8)	3.2 (94.1)	8.3 (86.0)	0.6 (91.7)	4.4 (95.5)	4.6 (91.4)
PGD	13.8 (83.5)	0.2 (96.7)	1.1 (86.2)	0.0 (100.0)	0.2 (96.7)	4.0 (74.0)	3.2 (89.5)
DDN	0.0 (0.2)	0.0 (0.0)	0.4 (0.8)	0.0 (0.4)	0.1 (0.8)	0.0 (0.3)	0.1 (0.4)
Cama	81.8 (91.3)	80.7 (85.3)	94.9 (98.3)	94.4 (97.1)	82.0 (93.5)	82.5 (95.3)	86.0 (93.5)

(b)

Attack	Preprocessor						Mean
	RGB	RGB+FD	FD	WW	CC	HP	
FGSM	8.7 (88.1)	0.1 (78.7)	1.9 (78.7)	6.9 (87.4)	1.1 (71.1)	8.5 (77.3)	4.5 (80.2)
PGD	10.8 (85.6)	0.1 (79.3)	0.4 (66.7)	0.0 (79.6)	0.0 (75.4)	4.5 (71.4)	2.6 (76.3)
DDN	0.2 (1.1)	0.0 (0.0)	0.0 (0.0)	0.0 (0.0)	0.0 (0.2)	0.1 (0.8)	0.1 (0.4)
Cama	86.6 (95.0)	96.5 (98.2)	95.5 (98.8)	95.6 (99.1)	83.6 (95.5)	92.1 (97.0)	91.7 (97.3)

Table 9. TSR (USR) in the *architecture transfer complete overlap* setting when anonymizing (a) in-distribution images (cf. Table 4a) and (b) out-of-distribution images (cf. Table 4b)

(a)

Attack		Preprocessor						Mean
		RGB	RGB+FD	FD	WW	CC	HP	
R-50	FGSM	16.7 (82.7)	16.6 (73.1)	15.6 (74.2)	18.5 (86.2)	17.0 (78.1)	18.2 (82.3)	17.1 (79.4)
	PGD	14.7 (67.1)	20.5 (74.5)	16.3 (81.6)	36.0 (75.0)	16.6 (81.6)	16.0 (80.2)	20.0 (76.7)
	DDN	0.1 (0.3)	0.0 (0.0)	0.0 (0.2)	0.0 (0.0)	0.0 (0.2)	0.0 (0.2)	0.0 (0.2)
	Cama	87.9 (92.3)	79.8 (83.7)	92.0 (92.5)	95.1 (95.9)	93.9 (95.9)	89.3 (89.9)	89.7 (91.7)
D-100	FGSM	17.5 (83.4)	16.6 (71.0)	16.0 (79.8)	18.0 (80.1)	16.4 (76.4)	19.0 (81.4)	17.2 (78.7)
	PGD	26.4 (59.2)	19.4 (71.1)	16.2 (79.4)	24.2 (77.9)	16.2 (79.7)	26.1 (74.6)	21.4 (73.6)
	DDN	0.0 (0.0)	0.0 (0.0)	0.0 (0.2)	0.0 (0.2)	0.0 (0.2)	0.1 (0.3)	0.0 (0.2)
	Cama	97.8 (98.7)	97.4 (97.8)	98.8 (99.3)	99.5 (99.8)	98.6 (98.9)	96.9 (99.5)	98.2 (99.0)
V-16	FGSM	19.8 (93.3)	16.2 (78.3)	16.0 (80.9)	16.7 (83.3)	16.7 (79.5)	21.4 (80.6)	17.8 (82.6)
	PGD	23.1 (77.7)	15.3 (77.1)	16.3 (81.1)	17.1 (83.4)	16.4 (80.3)	34.1 (76.3)	20.4 (79.3)
	DDN	0.4 (1.7)	0.1 (0.2)	0.0 (0.2)	0.3 (0.9)	0.0 (0.2)	0.0 (0.2)	0.1 (0.6)
	Cama	88.0 (95.9)	99.0 (99.3)	98.1 (98.8)	87.4 (96.6)	98.7 (99.3)	98.4 (98.8)	94.9 (98.1)

(b)

Attack		Preprocessor						Mean
		RGB	RGB+FD	FD	WW	CC	HP	
R-50	FGSM	20.3	25.7	17.8	22.1	18.2	19.5	20.6
	PGD	19.0	21.3	17.0	38.2	16.8	17.4	21.6
	DDN	16.9	18.4	18.2	18.1	18.3	18.6	18.1
	Cama	95.9	96.7	99.2	99.4	98.9	99.1	98.2
D-100	FGSM	19.4	26.1	18.7	21.9	19.9	31.7	23.0
	PGD	28.6	20.4	17.2	24.1	17.2	31.6	23.2
	DDN	16.9	18.3	19.4	19.4	17.4	18.2	18.3
	Cama	99.1	99.6	99.6	99.7	99.3	98.6	99.3
V-16	FGSM	19.6	19.0	17.6	16.8	19.1	35.1	21.2
	PGD	28.4	16.9	16.9	17.0	17.0	36.6	22.1
	DDN	17.4	17.2	17.2	17.6	19.3	17.7	17.7
	Cama	91.6	99.8	98.2	91.7	99.3	99.3	96.6

Table 10. TSR (USR) in the *architecture transfer partial overlap* setting when anonymizing (a) in-distribution images (cf. Table 5a) and (b) out-of-distribution images (cf. Table 5b)

(a)

		Preprocessor						
Attack		RGB	RGB+FD	FD	WW	CC	HP	Mean
R-50	FGSM	0.5 (96.9)	8.5 (86.2)	0.2 (97.6)	11.5 (85.2)	12.8 (86.0)	1.0 (95.4)	5.8 (91.2)
	PGD	0.2 (96.3)	5.6 (87.9)	0.0 (99.4)	16.1 (77.4)	6.6 (93.7)	0.5 (95.7)	4.8 (91.7)
	DDN	0.0 (0.3)	0.1 (6.5)	0.0 (0.2)	0.0 (0.2)	0.4 (4.5)	0.0 (0.7)	0.1 (2.1)
	Cama	92.6 (97.6)	73.3 (88.2)	83.3 (98.2)	91.9 (99.3)	81.9 (96.4)	75.3 (88.4)	83.0 (94.7)
	Mean							
D-100	FGSM	0.4 (98.3)	2.5 (96.5)	0.1 (99.5)	1.7 (100.0)	8.5 (86.5)	10.9 (81.5)	4.0 (93.7)
	PGD	2.3 (90.0)	2.7 (89.6)	0.0 (98.2)	0.3 (99.2)	0.8 (96.0)	16.1 (84.2)	3.7 (92.9)
	DDN	0.0 (0.0)	0.0 (0.0)	0.0 (0.1)	0.0 (0.0)	0.0 (0.2)	0.0 (0.2)	0.0 (0.1)
	Cama	88.3 (95.0)	96.7 (98.6)	96.3 (99.5)	96.9 (99.2)	88.9 (97.4)	88.9 (99.2)	92.7 (98.2)
	Mean							
V-16	FGSM	0.0 (99.8)	4.2 (87.4)	16.4 (81.9)	7.0 (96.4)	0.3 (97.9)	7.0 (85.8)	5.8 (91.5)
	PGD	0.0 (99.2)	1.0 (97.9)	15.9 (78.8)	0.8 (96.2)	0.2 (97.8)	5.2 (79.1)	3.8 (91.5)
	DDN	0.0 (0.0)	0.0 (0.0)	0.0 (0.1)	0.0 (0.1)	0.0 (0.2)	0.0 (0.2)	0.0 (0.1)
	Cama	98.3 (99.5)	95.1 (98.4)	94.5 (99.0)	94.3 (99.4)	97.3 (98.9)	92.9 (99.2)	95.4 (99.1)
	Mean							

(b)

		Preprocessor						
Attack		RGB	RGB+FD	FD	WW	CC	HP	Mean
R-50	FGSM	1.0 (76.4)	11.0 (92.5)	0.0 (78.6)	16.4 (91.9)	15.1 (95.5)	1.2 (76.1)	7.4 (85.2)
	PGD	0.3 (61.3)	7.8 (81.6)	0.0 (78.9)	16.8 (92.0)	4.7 (86.6)	0.0 (74.2)	4.9 (79.1)
	DDN	0.3 (1.8)	0.1 (1.5)	0.0 (0.2)	0.0 (0.0)	1.6 (15.6)	0.1 (0.4)	0.4 (3.2)
	Cama	96.1 (97.9)	88.4 (94.4)	88.7 (96.0)	97.5 (99.1)	81.3 (93.6)	86.8 (97.1)	89.8 (96.4)
	Mean							
D-100	FGSM	0.5 (77.1)	1.6 (83.1)	0.7 (78.5)	0.3 (80.6)	7.9 (80.6)	16.5 (85.4)	4.6 (80.9)
	PGD	1.2 (66.9)	2.4 (80.8)	0.0 (73.2)	0.1 (74.6)	0.2 (78.6)	16.0 (84.0)	3.3 (76.4)
	DDN	0.0 (0.0)	0.0 (0.0)	0.0 (0.0)	0.0 (0.0)	0.0 (0.0)	0.0 (0.2)	0.0 (0.0)
	Cama	92.3 (95.5)	97.8 (98.5)	95.2 (98.3)	97.3 (98.8)	91.2 (95.6)	94.7 (98.0)	94.8 (97.4)
	Mean							
V-16	FGSM	0.1 (81.8)	5.6 (82.6)	17.1 (98.1)	2.5 (80.4)	0.1 (77.1)	11.1 (74.0)	6.1 (82.3)
	PGD	0.1 (79.3)	0.6 (81.6)	16.8 (99.4)	0.1 (79.2)	0.1 (78.8)	4.6 (66.9)	3.7 (80.9)
	DDN	0.0 (0.0)	0.0 (0.0)	0.0 (0.0)	0.0 (0.0)	0.0 (0.2)	0.0 (0.0)	0.0 (0.0)
	Cama	98.9 (99.6)	97.6 (98.8)	93.0 (97.4)	95.4 (97.5)	96.4 (98.8)	95.9 (97.9)	96.2 (98.3)
	Mean							